LETTER

doi:10.1038/nature16484

A lithium–oxygen battery based on lithium superoxide

Jun Lu[1]*, Yun Jung Lee[2]*, Xiangyi Luo[3,4]*, Kah Chun Lau[3]*, Mohammad Asadi[5]*, Hsien-Hau Wang[3], Scott Brombosz[3], Jianguo Wen[6], Dengyun Zhai[1], Zonghai Chen[1], Dean J. Miller[6], Yo Sub Jeong[2], Jin-Bum Park[2], Zhigang Zak Fang[4], Bijandra Kumar[7], Amin Salehi-Khojin[5], Yang-Kook Sun[2], Larry A. Curtiss[3] & Khalil Amine[1]

Batteries based on sodium superoxide and on potassium superoxide have recently been reported[1–3]. However, there have been no reports of a battery based on lithium superoxide (LiO_2), despite much research[4–8] into the lithium–oxygen (Li–O_2) battery because of its potential high energy density. Several studies[9–16] of Li–O_2 batteries have found evidence of LiO_2 being formed as one component of the discharge product along with lithium peroxide (Li_2O_2). In addition, theoretical calculations have indicated that some forms of LiO_2 may have a long lifetime[17]. These studies also suggest that it might be possible to form LiO_2 alone for use in a battery. However, solid LiO_2 has been difficult to synthesize in pure form[18] because it is thermodynamically unstable with respect to disproportionation, giving Li_2O_2 (refs 19, 20). Here we show that crystalline LiO_2 can be stabilized in a Li–O_2 battery by using a suitable graphene-based cathode. Various characterization techniques reveal no evidence for the presence of Li_2O_2. A novel templating growth mechanism involving the use of iridium nanoparticles on the cathode surface may be responsible for the growth of crystalline LiO_2. Our results demonstrate that the LiO_2 formed in the Li–O_2 battery is stable enough for the battery to be repeatedly charged and discharged with a very low charge potential (about 3.2 volts). We anticipate that this discovery will lead to methods of synthesizing and stabilizing LiO_2, which could open the way to high-energy-density batteries based on LiO_2 as well as to other possible uses of this compound, such as oxygen storage.

The crystalline LiO_2 reported here was made electrochemically using a cathode based on reduced graphene oxide (rGO) with added iridium (Ir) nanoparticles. Initially graphene oxide (GO) was prepared by a modified Hummer's method[21,22]. The Ir–rGO composite was then made by a hydrothermal reduction method and characterized (Supplementary Fig. 2). Scanning electron microscopy (SEM) images of the pristine rGO and Ir–rGO composite (Fig. 1a and b, respectively) reveal porous three-dimensional (3D) networks of rGO composed of wrinkled 2D rGO sheets. Figure 1c and d shows transmission electron microscopy (TEM) images of the Ir nanoparticles on rGO, indicating that the well-dispersed Ir nanoparticles decorated on rGO are very small (<2 nm), with evidence for the presence of some small Ir clusters (circled in Fig. 1d). A backscattering image (Supplementary Fig. 1) shows some scattered larger Ir particles of about 500 nm in size, which may be due to agglomeration of the smaller nanoparticles, and fast Fourier transform analysis of high-resolution (HR)-TEM images (Supplementary Fig. 1) show that the nanoparticles are Ir. An X-ray photoemission spectroscopy (XPS) analysis (Supplementary Fig. 1) indicates the Ir surface is only partially oxidized.

The performance of the rGO and Ir–rGO cathodes was examined using a Swagelok-type cell composed of a lithium metal anode, electrolyte (1 M $LiCF_3SO_3$ in tetraethylene glycol dimethyl ether (TEGDME)) impregnated into a glass fibre separator, and a porous cathode. A current density of 100 mA g^{-1} was used for both discharge and charge, and the cell was run with a capacity limit of 1,000 mA h g^{-1} to avoid side reactions. The specific capacity (mA h g^{-1}) and the current density (mA g^{-1}) are based on the active materials of the O_2 electrodes. Figure 2a and b shows voltage profiles for the Ir–rGO and rGO cathode architectures, respectively. The Ir–rGO discharge product shows a very low charge potential of ~3.2 V that rises to 3.5 V over 40 cycles leading to more than 85% efficiency in this system (Fig. 2a). The voltage profile of the rGO cathode shows a much larger charge potential of ~4.2 V with a lower efficiency of ~67% (Fig. 2b).

The discharge product resulting from the Ir–rGO cathode was examined using SEM, differential electrochemical mass spectroscopy (DEMS), high-energy X-ray diffraction (HE-XRD), TEM and Raman spectroscopy with the results shown in Figs 2 and 3. The SEM image in Fig. 2c shows the Ir–rGO cathode after discharge (~2.75 V) from the first cycle (1,000 mA h g^{-1} capacity). This image indicates that the discharge product resulting from the Ir–rGO-based cathode consists mainly of nanoparticles with needle- or rod-like morphology, although the presence of other shapes such as cubic cannot be ruled out. This needle- or rod-like morphology is also observed in the TEM image of a part of the discharge product, which appears to be on the surface of the Ir–rGO nanostructures (Fig. 2c inset). An SEM image after charging shows that the nanoparticles have disappeared (Supplementary Fig. 3). The discharge product from the rGO-based cathode has a range of morphologies, including toroids and nanoparticles (Supplementary Fig. 3). The Ir–rGO discharge product produced by a current density of 100 mA g^{-1} was characterized by DEMS during the first charging cycle by on-line monitoring of the number of evolved O_2 molecules. The experiment was performed using high current densities (1,000 mA g^{-1} and 640 mA g^{-1}) for charging to enable measurement of the evolved O_2. The DEMS results at the higher current density are shown in Fig. 2d. Analysis of the data in Fig. 2d gives an average O_2 formation rate of 1.3×10^{-9} mol s^{-1}, resulting in an e^-/O_2 ratio of 1.00. A similar (1.00) e^-/O_2 ratio was also obtained for the experiment with a current density of 640 mA g^{-1} (Supplementary Fig. 18). Additionally, negligible amounts of CO_2 and H_2 gases were generated during the DEMS experiments (Fig. 2d and Supplementary Fig. 18). A DEMS experiment was also carried out during discharge, and gave an e^-/O_2 ratio of 1.02 (Supplementary Fig. 18, Supplementary Table 3). These results are consistent with LiO_2 as the main discharge product, and provide evidence for the absence of other products (for example, Li_2O_2, LiOH and Li_2CO_3). The DEMS results for LiO_2 are similar to DEMS measurements on a NaO_2 battery that gave an e^-/O_2 ratio of 1.00 for discharge and 1.02 for charge[2].

[1]Chemical Sciences and Engineering Division, Argonne National Laboratory, Argonne, Illinois 60439, USA. [2]Department of Energy Engineering, Hanyang University, Seoul 133-791, South Korea. [3]Materials Science Division, Argonne National Laboratory, Argonne, Illinois 60439, USA. [4]Department of Metallurgical Engineering, University of Utah, Salt Lake City, Utah 84112, USA. [5]Department of Mechanical and Industrial Engineering, University of Illinois at Chicago, Chicago, Illinois 60607, USA. [6]Center for Nanoscale Materials, Argonne National Laboratory, Argonne, Illinois 60439, USA. [7]Conn Center for Renewable Energy Research, University of Louisville, Louisville, Kentucky 40292, USA.
*These authors contributed equally to this work.

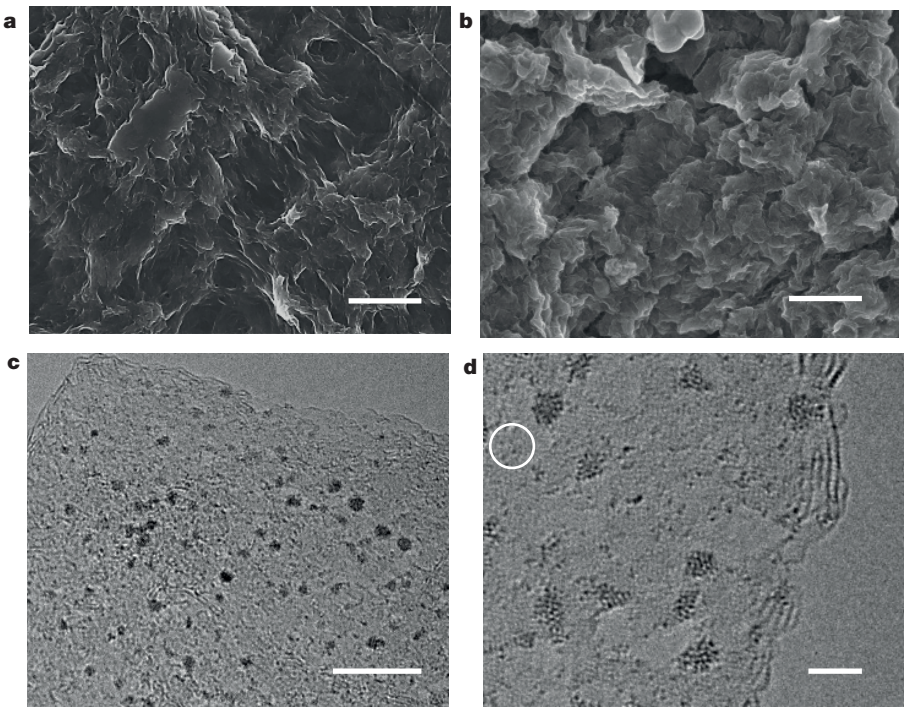

Figure 1 | Morphology of Ir–rGO. a, SEM image of pristine rGO powder. **b**, SEM image of Ir–rGO composite. **c**, **d**, TEM images of Ir-rGO composite, showing Ir nanoparticles less than 2 nm in size. The circle in **d** shows some small Ir atomic clusters. Scale bars: **a**, **b**, 1 μm; **c**, 10 nm; **d**, 2 nm. There are also some scattered large Ir agglomerates on the rGO (see Supplementary Fig. 1).

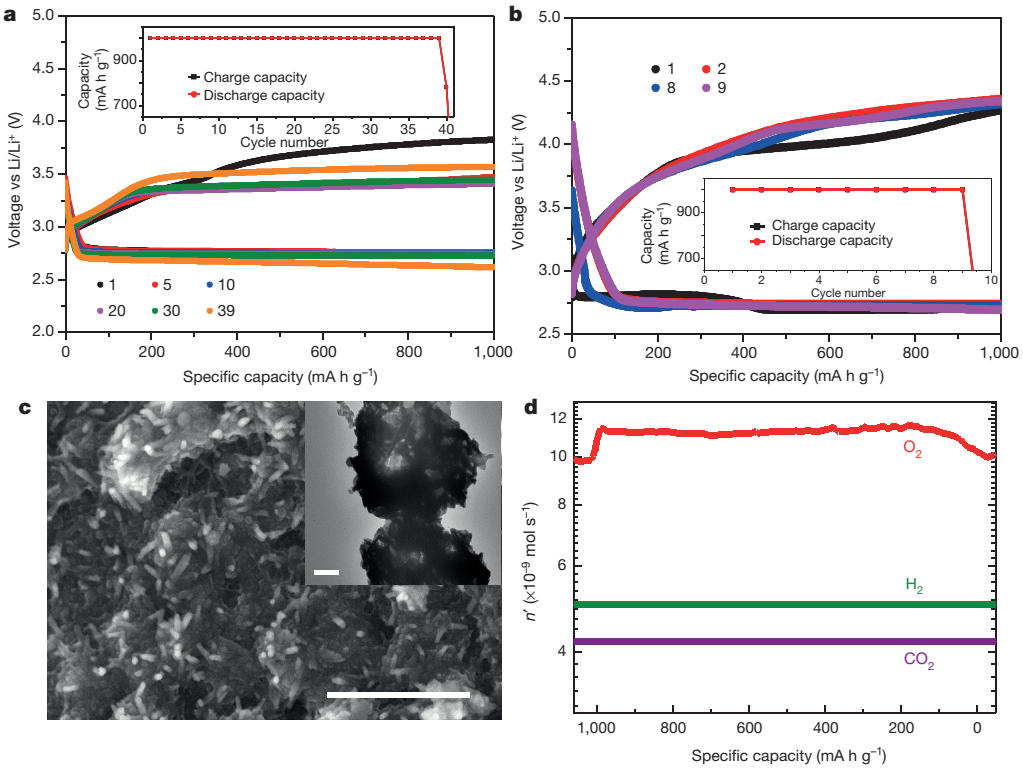

Figure 2 | Electrochemical tests and discharge products. a, Voltage profiles of the Ir–rGO cathode (see also Supplementary Fig. 6). Cycle number of voltage plot is given by the colour of the plotting symbol (see key). Inset shows capacity as a function of cycle number. **b**, Voltage profiles of the rGO cathode. Cycle number of voltage plot is given by the colour of the plotting symbol (see key). Inset shows capacity as a function of cycle number. **c**, Main panel, SEM image of discharge product on Ir–rGO (scale bar, 1 μm); inset, TEM image of discharge product on Ir–rGO (scale bar, 200 nm). Both main panel and inset are from the first discharge with a current density of 100 mA g^{-1}, and capacity control of 1,000 mAh g^{-1}. **d**, DEMS profile showing O_2, H_2 and CO_2 gases released (n' is the number of moles per second) from the cell during the charging process (at 1,000 mA g^{-1} current density) after the first discharge (at 100 mA g^{-1} current density) to 1,000 mA h g^{-1} capacity (see Supplementary Information for details).

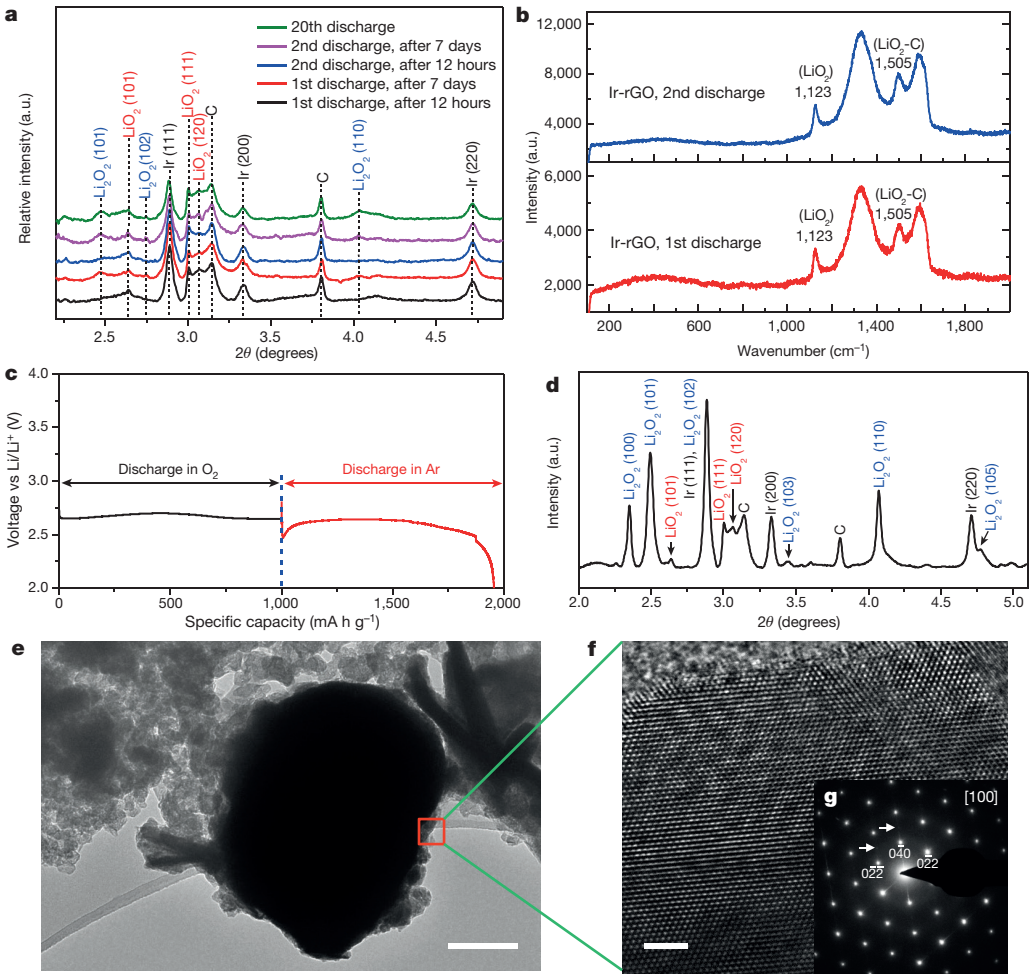

Figure 3 | Characterization of discharge products. a, HE-XRD patterns of discharge product on Ir–rGO as a function of ageing time. **b**, Raman spectra of discharge product on Ir–rGO for first and second discharges. **c**, Voltage plots for Ir–rGO discharged first in O_2 to a capacity of 1,000 mA h g^{-1} and then discharged in Ar during which time it attained a capacity 956 mA h g^{-1}; in the latter case, the electrolyte was purged with Ar before discharge (see Supplementary Fig. 16 for comparison with other cathode materials). **d**, HE-XRD pattern of cathode resulting from both discharges in **c**. **e**–**g**, TEM image of an Ir agglomerate after first discharge (**e**; scale bar, 200 nm); **f**, HR-TEM image of boxed area in **e** (scale bar, 2 nm); and **g**, the corresponding electron diffraction pattern along the [100] zone axis giving evidence for the formation of an Ir_3Li intermetallic. The indices are diffraction vectors. Weak superstructure is observed as indicated by arrows.

The HE-XRD pattern in Fig. 3a for the discharge product on the Ir–rGO cathode (1,000 mA h g^{-1} capacity) during the first cycle shows peaks corresponding to crystalline LiO_2 ((101), (111), (120)), and no evidence for peaks corresponding to Li_2O_2. The identification of the LiO_2 peaks is based on a theoretical XRD pattern derived from the DFT (density functional theory)-predicted crystalline LiO_2 structure (Supplementary Fig 4) from refs 19 and 23, as no experimental XRD pattern has been reported. The LiO_2 structure is orthorhombic (Supplementary Fig. 4). For comparison, NaO_2 is cubic at room temperature and orthorhombic at <196 K, whereas KO_2 is tetragonal at room temperature. Some amorphous LiO_2 cannot be ruled out on the basis of the XRD results. The standard XRD pattern of Li_2O_2 was used to determine the absence of Li_2O_2. The Raman spectra of the discharge product of the Ir–rGO cathode in Fig. 3b show the presence of a peak at 1,123 cm^{-1}, consistent with the range of values that have been observed for superoxide stretching frequencies (Supplementary Table 1). It is also consistent with the Raman peak at 1,156 cm^{-1} observed[1] for NaO_2. There is also a peak at 1,505 cm^{-1} that has recently been attributed to the strong interaction between LiO_2 and a graphitic carbon surface[9]. In contrast, the HE-XRD pattern (Supplementary Fig. 3) for the discharge product on the rGO cathode without Ir added (1,000 mA h g^{-1} capacity) during the first cycle shows peaks corresponding to both crystalline LiO_2 ((101), (111), (120)) and Li_2O_2 ((101), (102), (103), (110)). Evidence for both LiO_2 and Li_2O_2 components in the discharge product has also been reported in other studies[9–15], although none are based on XRD characterization, which is made possible by the use of high-energy X-rays at the Advanced Photon Source of Argonne National Laboratory. When the Ir–rGO cell is run to deep discharge of 2.2 V and ~9,500 mA h g^{-1} capacity, the HE-XRD data shows evidence for the presence of LiO_2, Li_2O_2 and LiOH with a toroidal morphology (Supplementary Fig. 5).We also note that there have been some previous studies[24,25] on rGO and rGO with Au nanoparticles that showed formation of Li_2O_2, but no report of LiO_2 in a Li–O_2 cell.

Further evidence that the discharge product is LiO_2 on the Ir–rGO cathode was obtained by an experiment in which Li was electrochemically added to the discharge product without the presence of O_2 (that is, O_2 was replaced by Ar). The voltage profile is shown in Fig. 3c for this discharge process, along with that of the initial discharge process (to 1,000 mA h $^{-1}$g). The HE-XRD of the resulting product with no O_2 in the cell is shown in Fig. 3d and reveals strong peaks from Li_2O_2, thus indicating a conversion of LiO_2 to Li_2O_2 ($Li^+ + e^- + LiO_2 \rightarrow Li_2O_2$) with ~96% of the theoretical capacity for this reaction attained. This is evidence for a reaction involving one electron per O_2 in the first cycle for 1,000 mA h g^{-1} capacity, and for no crystalline or amorphous Li_2O_2 forming on the initial capacity-limited discharge. In contrast, no significant capacity for discharge in Ar is observed for the rGO cathode when a similar procedure is performed. We have also carried

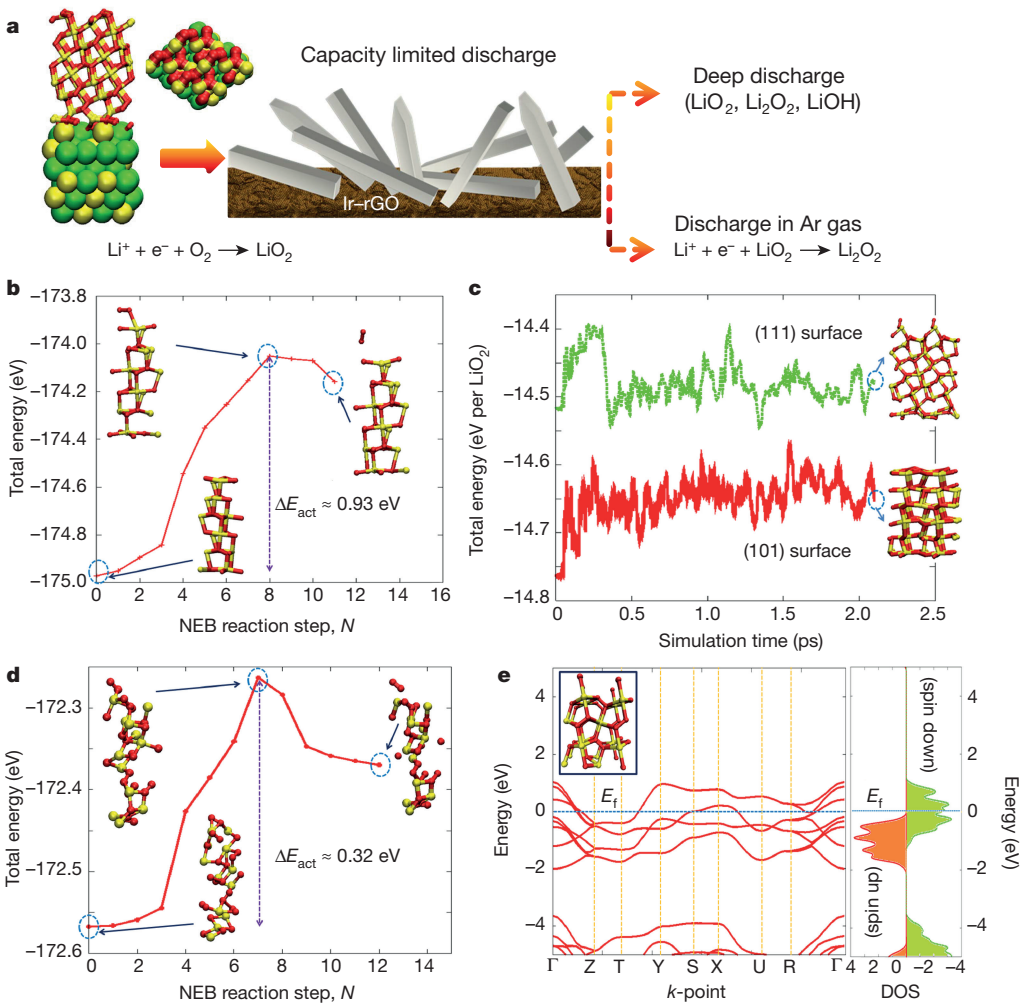

Figure 4 | Density functional calculations. a, Schematic showing lattice match between LiO_2 and Ir_3Li (see also Supplementary Fig. 13) that may be responsible for the LiO_2 discharge product found on the Ir–rGO cathode. The two structures at left are the side- and top-views representing epitaxial growth of crystalline LiO_2 in (111) orientation on a (121) facet of Ir_3Li (Li is yellow, O is red and Ir is green). The rod-like structures shown in the central figure are schematic representations of the crystalline LiO_2 morphology observed in the experiment. Two subsequent electrochemical reactions that the LiO_2 can undergo are shown on the right: that is, either further lithiation in the presence of Ar or further oxygen reduction in the presence of oxygen. **b**, DFT calculations of the barrier for desorption (ΔE_{act}) of an O_2 molecule from the (101)LiO_2 surface in vacuum from a Nudged Elastic Band (NEB) calculation as a function of number of reaction steps, *N*. **c**, AIMD simulations of (111)LiO_2 and (101)LiO_2 surfaces in vacuum at room temperature. **d**, DFT calculations of the barrier for desorption of an O_2 molecule from an amorphous LiO_2 surface in vacuum. **e**, DFT electronic band structure (left) and density of states (DOS) plot (right) of ferromagnetic bulk crystalline LiO_2 close to the Fermi level (E_f) based on a spin polarized calculation with electronic spin-up and spin-down states shown. (See also Supplementary Fig. 17.)

out electron paramagnetic resonance (EPR) measurements, and find a signal that is consistent with the presence of LiO_2 (Supplementary Fig. 7, Supplementary Table 2) in the initial discharge product.

The stability of the LiO_2 was investigated by carrying out HE-XRD measurements on Ir–rGO cathodes aged for different times in the presence of the electrolyte (Fig. 3a). After 12 hours at the end of both the first and second discharges the XRD patterns show only evidence for crystalline LiO_2. When the discharge product is allowed to remain for seven days under the same conditions, both samples still show the signature of LiO_2 along with the presence of crystalline Li_2O_2. Thus, the HE-XRD measurements indicate that the crystalline LiO_2 formed with the Ir–rGO cathode is surprisingly stable for a relatively long period of time. Raman spectra (Supplementary Fig. 8) measured as a function of time exhibit a decreasing intensity of the peak at 1,123 cm^{-1} as a function of time, which is consistent with the HE-XRD results. In addition, LiO_2 is still the dominant discharge product on the twentieth discharge cycle, indicating that LiO_2 is stable enough that it can be repeatedly charged and discharged for about 40 cycles with a very low charge potential (~3.2 V); this may open the way to a lithium-superoxide-based battery.

An explanation of the formation mechanism and stability of the LiO_2 found in this study requires an understanding of the growth and nucleation process, which is quite complex and beyond the scope of the present study. However, our results are consistent with mechanisms proposed in other recent studies. Some insight can be obtained from a postulated mechanism for the nucleation and growth of discharge products from various size-specific Ag clusters decorating carbon cathodes in a $Li–O_2$ cell[7]. In that case, the results are explained by a through-solution growth mechanism with sites for oxygen reduction reactions (ORRs) that are separate from the nucleation sites. Other researchers have also reported evidence for through-solution mechanisms[26–29]. In addition, the results of the Ag cluster study[7] suggest that availability of good ORR sites promotes a through-solution mechanism involving nucleation and growth of LiO_2 followed by disproportionation to Li_2O_2. Since both Ir and rGO are good ORR materials[30,31], the Ir–rGO-based cathodes of the present study should result in a similar mechanism, that is, initial formation of LiO_2.

The HE-XRD finding that rGO results in both LiO_2 and Li_2O_2 in the discharge product can be accounted for by slow disproportionation. This explanation is supported by a recent theoretical study[17] that has

shown the possibility of fast and slow disproportionation processes for LiO_2 depending on the LiO_2 cluster size. In addition, experimental evidence for slow disproportionation has been found in studies of Li–O_2 cell discharge products based on an activated carbon cathode[10]. In contrast, the present HE-XRD results showing that only LiO_2 is present in the case of the Ir–rGO-based cathode material suggest that disproportionation is suppressed.

The formation of only LiO_2 in the case of the present Ir–rGO cathode may be due to some aspect of that cathode that favours nucleation and growth of largely the crystalline LiO_2 phase, which prevents disproportionation (see theoretical calculations below). In the case of Ir–rGO, we noticed the formation of an Ir_3Li intermetallic compound on the large Ir agglomerates seen in the backscattering image (Supplementary Fig. 1), as shown Fig. 3f and g). We also noticed that some nanoparticles (needle or rod-like) are formed on the surface of these agglomerates during the first discharge (Fig. 3e). We note that the Ir_3Li intermetallic compound has an orthorhombic lattice, a similar crystallographic lattice[32] to that of LiO_2. It is possible that it may act as a template for growth of the crystalline LiO_2, as has been found in template-controlled nucleation and growth of other crystalline materials[33]. We carried out DFT calculations on the interface between LiO_2 and Ir_3Li, and found that some crystalline faces had good lattice matches (Supplementary Fig. 13), as would be required for epitaxial growth of crystalline LiO_2. There may be other intermetallic compounds that exhibit similar behaviour and will be the subject of further study. The schematic in Fig. 4 summarizes the novel templating process that may be responsible for the LiO_2 discharge product found for the Ir-rGO cathode material and the subsequent electrochemical reactions that it can undergo, that is, either further lithiation or further oxygen reduction. In contrast, the rGO cathode, which does not include Ir nanoparticles, probably has a different nucleation and growth mechanism resulting in a discharge product composed of both LiO_2 and Li_2O_2.

The kinetic stability of crystalline and amorphous LiO_2 was investigated using *ab initio* molecular dynamics (AIMD) and DFT calculations with the results shown in Fig. 4. The disproportionation rate will depend on several factors. One factor is the rate at which the O_2 leaves the surface. The DFT results in Fig. 4b indicate that the initial step of O_2 leaving the crystalline surface into vacuum has a barrier of ~0.9 eV based on a low-energy LiO_2 surface. Figure 4c shows that crystalline LiO_2 surfaces (that is, (101) and (111)) are thermally stable in vacuum at room temperature. For an amorphous surface, the barrier (~0.3 eV) is less than for the crystalline surface (Fig. 4d). From AIMD simulations, the presence of some solvent molecules adsorbed on the amorphous LiO_2 surface reduces O_2 desorption (Supplementary Fig. 14). This suggests that solvent on the LiO_2 surface could further suppress disproportionation of the crystalline phase. The electrolyte effect on disproportionation was investigated by allowing a sample from a 1,000 mA h g^{-1} discharge to age for 24 h in vacuum. Characterization of the sample by Raman spectroscopy, discharge in Ar, and charge potential shows a significant decrease of LiO_2 signature after ageing in vacuum, indicating that kinetics plays an important role in stabilizing the LiO_2 (Supplementary Fig. 15)

The Ir–rGO cathode also exhibits a low charge potential, which may be due to several factors. As shown in Fig. 4e, crystalline LiO_2 is a half-metal (on the basis of density functional calculations) and, thus, will have good electronic conduction, in contrast to insulating bulk Li_2O_2. Another factor is that Ir is known to be a good oxygen evolution catalyst[31] and interacts strongly with LiO_2 to form a good interface for electrical contact. These properties may explain why the discharge product formed on just rGO has a large charge potential, that is, it lacks the Ir nanoparticles. The Li–O_2 cell based on Ir–rGO cathode material also can cycle 40 or more times (Supplementary Fig. 9) before failure, similar to what has been found for Li_2O_2-based Li–O_2 cells, indicating that the lithium superoxide is not any more reactive towards the electrolyte than lithium peroxide. In addition, the low charge potential will lead to less side reactions. The failure of the cell could be due to oxygen crossover to the anode resulting in the anode being converted to LiOH, as evidenced by the corrosion of the anode (Supplementary Fig. 10) and, possibly the poisoning of Ir metal catalyst with cycling. When the cycled Li anode is replaced by a new anode, the cell cycles another 30 times (Supplementary Fig. 10).

The evidence presented here indicates that a Li–O_2 electrochemical cell based on a LiO_2 discharge product is possible with a reasonable cycle life, very high efficiency, and a good capacity. The performance characteristics of the cell based on LiO_2 are comparable to those of previously reported electrochemical cells based on KO_2 (ref. 3) and on NaO_2 (ref. 1), although some aspects—such as the charge and discharge potentials—differ. Problems with electrolyte stability and decomposition, as for the electrolytes used for other Li–O_2 systems, probably still remain, but they do not seem any worse than for those systems. There is little evidence of any side reactions in the Raman data for the first discharge cycle (Fig. 3b), or from Raman and Fourier transform infrared data after charging for up to 30 cycles (Supplementary Figs 11, 12), or from NMR data up to 20 cycles (Supplementary Fig. 12), although there could be decomposition products that are not detected. The Fourier transform infrared and Raman results also confirm that the discharge product is not present after charging.

In summary, we have reported evidence it is possible to have a one-electron discharge process that forms only LiO_2 in a Li–O_2 electrochemical cell. This is different from the previous studies[9–15] that have provided evidence for both LiO_2 and Li_2O_2 in the discharge product of Li–O_2 batteries with some cathode and electrolyte materials, and from studies[16] that have shown LiO_2 can be present in solution during discharge. The evidence for the existence of the LiO_2 comes from DEMS and HE-XRD data with no evidence for Li_2O_2 being present. The results of TEM and density functional calculations indicate that a novel templating growth mechanism involving the use of Ir nanoparticles may be responsible for the crystalline LiO_2 growth. The LiO_2 formed in this way is stable enough to be repeatedly charged and discharged with a very low charge overpotential.

Online Content Methods, along with any additional Extended Data display items and Source Data, are available in the online version of the paper; references unique to these sections appear only in the online paper.

Received 1 October 2014; accepted 13 November 2015.
Published online 11 January 2016.

1. Hartmann, P. *et al.* A rechargeable room-temperature sodium superoxide (NaO_2) battery. *Nature Mater.* **12,** 228–232 (2012).
2. Hartmann, P. *et al.* A comprehensive study on the cell chemistry of the sodium superoxide (NaO_2) battery. *Phys. Chem. Chem. Phys.* **15,** 11661–11672 (2013).
3. Ren, X. & Wu, Y. A low-overpotential potassium–oxygen battery based on potassium superoxide. *J. Am. Chem. Soc.* **135,** 2923–2926 (2013).
4. Lu, J. *et al.* A nanostructured cathode architecture for low charge overpotential in lithium-oxygen batteries. *Nature Commun.* **4,** 2383 (2013).
5. Bruce, P. G., Freunberger, S. A., Hardwick, L. J. & Tarascon, J.-M. Li-O_2 and Li-S batteries with high energy storage. *Nature Mater.* **11,** 19–29 (2011).
6. Lu, J. *et al.* Aprotic and aqueous Li–O_2 batteries. *Chem. Rev.* **114,** 5611–5640 (2014).
7. Lu, J. *et al.* Effect of the size-selective silver clusters on lithium peroxide morphology in lithium–oxygen batteries. *Nature Commun.* **5,** 4895 (2014).
8. Black, R., Lee, J.-H., Adams, B., Mims, C. A. & Nazar, L. F. The role of catalysts and peroxide oxidation in lithium–oxygen batteries. *Angew. Chem. Int. Edn* **52,** 392–396 (2013).
9. Zhai, D. *et al.* Raman evidence for late stage disproportionation in a Li–O_2 battery. *J. Phys. Chem. Lett.* **5,** 2705–2710 (2014).
10. Zhai, D. *et al.* Disproportionation in Li–O_2 batteries based on a large surface area carbon cathode. *J. Am. Chem. Soc.* **135,** 15364–15372 (2013).
11. Yang, J. *et al.* Evidence for lithium superoxide-like species in the discharge product of a Li-O_2 battery. *Phys. Chem. Chem. Phys.* **15,** 3764–3771 (2013).
12. Gittleson, F. S., Ryu, W.-H. & Taylor, A. D. Operando observation of the gold-electrolyte interface in Li-O_2 batteries. *ACS Appl. Mater. Interfaces* **6,** 19017–19025 (2014).
13. Gittleson, F. S. *et al.* Raman spectroscopy in lithium-oxygen battery systems. *ChemElectroChem* **2,** 1446–1457 (2015).

14. Olivares-Marín, M. *et al.* Spatial distributions of discharged products of lithium-oxygen batteries revealed by synchrotron X-ray transmission microscopy. *Nano Lett.* **15,** 6932–6938 (2015).
15. Ryu, W.-H., Gittleson, F. S., Schwab, M., Goh, T. & Taylor, A. D. A mesoporous catalytic membrane architecture for lithium-oxygen battery systems. *Nano Lett.* **15,** 434–441 (2015).
16. Schaltin, S., Vanhoutte, G., Wu, M., Bardé, F. & Fransaer, J. A QCM study of ORR-OER and an in situ study of a redox mediator in DMSO for Li-O_2 batteries. *Phys. Chem. Chem. Phys.* **17,** 12575–12586 (2015).
17. Das, U., Lau, K. C., Redfern, P. C. & Curtiss, L. A. Structure and stability of lithium superoxide clusters and relevance to Li–O_2 batteries. *J. Phys. Chem. Lett.* **5,** 813–819 (2014).
18. Sangster, J. & Pelton, A. D. The Li-O (lithium-oxygen) system. *J. Phase Equilibria* **13,** 296–299 (1992).
19. Lau, K. C., Curtiss, L. A. & Greeley, J. Density functional investigation of the thermodynamic stability of lithium oxide bulk crystalline structures as a function of oxygen pressure. *J. Phys. Chem. C* **115,** 23625–23633 (2011).
20. Kang, S., Mo, Y., Ong, S. P. & Ceder, G. A facile mechanism for recharging Li_2O_2 in Li–O_2 batteries. *Chem. Mater.* **25,** 3328–3336 (2013).
21. Hummers, W. S. & Offeman, R. E. Preparation of graphitic oxide. *J. Am. Chem. Soc.* **80,** 1339 (1958).
22. Xu, Y., Sheng, K., Li, C. & Shi, G. Self-assembled graphene hydrogel via a one-step hydrothermal process. *ACS Nano* **4,** 4324–4330 (2010).
23. Zhuravlev, Y. N. & Obolonskaya, O. S. Structure, mechanical stability, and chemical bond in alkali metal oxides. *J. Struct. Chem.* **51,** 1005–1013 (2010).
24. Kumar, S., Selvaraj, C., Munichandraiah, N. & Scanlon, L. G. Gold nanoparticles anchored reduced graphene oxide as catalyst for oxygen electrode of rechargeable Li-O_2 cells. *RSC Adv.* **3,** 21706–21714 (2013).
25. Selvaraj, C., Kumar, S., Munichandraiah, N. & Scanlon, L. G. Reduced graphene oxide-polypyrrole composite as a catalyst for oxygen electrode of high rate rechargeable Li-O_2 cells. *J. Electrochem. Soc.* **161,** A554–A560 (2014).
26. Oh, S. H., Black, R., Pomerantseva, E., Lee, J.-H. & Nazar, L. F. Synthesis of a metallic mesoporous pyrochlore as a catalyst for lithium–O_2 batteries. *Nature Chem.* **4,** 1004–1010 (2012).
27. Ren, X., Zhang, S. S., Tran, D. T. & Read, J. Oxygen reduction reaction catalyst on lithium/air battery discharge performance. *J. Mater. Chem.* **21,** 10118–10125 (2011).
28. Mitchell, R. R., Gallant, B. M., Shao-Horn, Y. & Thompson, C. V. Mechanisms of morphological evolution of Li_2O_2 particles during electrochemical growth. *J. Phys. Chem. Lett.* **4,** 1060–1064 (2013).
29. Ottakam Thotiyl, M. M., Freunberger, S. A., Peng, Z. & Bruce, P. G. The carbon electrode in nonaqueous Li–O_2 cells. *J. Am. Chem. Soc.* **135,** 494–500 (2013).
30. Bikkarolla, S. K., Cumson, P., Joseph, P. & Papakonstantinou, P. Oxygen reduction reaction in electrochemically reduced graphene oxide. *Faraday Discuss.* **173,** 415–428 (2014).
31. Antolini, E. Iridium as catalyst and cocatalyst for oxygen evolution/reduction in acidic polymer electrolyte membrane electrolyzers and fuel cells. *ACS Catal.* **4,** 1426–1440 (2014).
32. Donkersloot, H. C. & Van Vucht, J. H. N. The crystal structure of IrLi, Ir_3Li and $LiRh_3$. *J. Less Common Met.* **50,** 279–282 (1976).
33. Pouget, E. M. *et al.* The initial stages of template-controlled $CaCO_3$ formation revealed by cryo-TEM. *Science* **323,** 1455–1458 (2009).

Supplementary Information is available in the online version of the paper.

Acknowledgements This work was primarily supported by the US Department of Energy under contract DE-AC02-06CH11357 from the Vehicle Technologies Office, Department of Energy, Office of Energy Efficiency and Renewable Energy. We also acknowledge support from the Center for Electrochemical Energy Science (CEES), an Energy Frontier Research Center (EFRC) funded by the US Department of Energy, Office of Science, Office of Basic Energy Sciences (X-ray measurements and analysis). We also acknowledge support from the University of Illinois-Chicago Chancellor Proof of Concept Fund (DEMS measurements). We acknowledge the Conn Renewable Energy Research Center at the University of Louisville for providing the access to the DEMS equipment. We acknowledge grants of computer time through INCITE awards on the BlueGene/Q computer at Argonne National Laboratory and allocations on the CNM Carbon Cluster at Argonne National Laboratory and the LCRC Fusion Cluster at Argonne National Laboratory. Use of the Advanced Photon Source and the Electron Microscopy Center, Center for Nanoscale Materials was supported by the US Department of Energy, Office of Basic Energy Sciences, under contract no. DE-AC02-06CH11357. We acknowledge financial support from the Human Resources Development of the Korea Institute of Energy Technology Evaluation and Planning (KETEP) funded by the Korea government Ministry of Knowledge Economy (no. 20124010203310), and from the Basic Science Research Program (no. NRF-2014R1A2A1A11049801). We acknowledge C. Barile, R. Rooney, R. Assary and P. Redfern for discussions and help on the lithium superoxide reaction mechanism.

Author Contributions J.L. and K.A. designed the experiments; Y.J.L., J.-B.P. and Y.S.J. synthesized the cathode materials; J.L., D.J.M. and J.W. performed and analysed the TEM imaging experiments; J.L., X.L., L.A.C. and Z.C. performed and analysed the X-ray measurements; J.L., X.L., Z.Z.F., D.Z. and H.-H.W. tested the cathode materials; M.A., A.S.-K. and B.K. performed the DEMS measurements, H.-H.W., X.L. and S.B. performed the Raman, NMR, EPR and FTIR experiments, K.C.L. and L.A.C. were responsible for the theoretical computations. L.A.C., K.A. and Y.-K.S. supervised the project; L.A.C., J.L. and K.A. wrote the paper. All of the authors discussed the results and reviewed the manuscript.

Author Information Atomic coordinates for the LiO_2 crystal structure from DFT can be obtained from the ICSD Database (http://www2.fiz-karlsruhe.de/icsd_home.html). Reprints and permissions information is available at www.nature.com/reprints. The authors declare no competing financial interests. Readers are welcome to comment on the online version of the paper. Correspondence and requests for materials should be addressed to L.A.C. (curtiss@anl.gov) or K.A. (amine@anl.gov) or Y.-K.S. (yksun@hanyang.ac.kr).

METHODS

Material preparation. Graphene oxide (GO) was prepared by a modified Hummers method[21,22]. Pristine reduced GO (rGO) was produced by reducing GO in polyol[34]. Specifically, a GO dispersion (1 mg ml^{-1}) in ethylene glycol (EG) was first prepared with the aid of horn sonication for 1 h. The solution pH was then adjusted to pH 13 with NaOH (2.5 M in EG). The reaction temperature was increased to 120 °C, and a reducing agent ($NaBH_4$) dissolved in EG was injected slowly. The solution was allowed to react for 1 h at this temperature and then cooled to room temperature. The precipitate was filtered, washed and dried under vacuum. The Ir–rGO composite was synthesized by a hydrothermal method. $IrCl_3 \bullet H_2O$ was added to 100 ml aqueous GO solution (0.67 mg ml^{-1}) with a weight ratio of $IrCl_3 \bullet H_2O$ to GO of 1.9:1. The mixture was stirred for 2 h. The resulting solution was transferred to a Teflon-lined autoclave and there reacted hydrothermally at 180 °C for 12 h. The precipitate was filtered, washed and dried under vacuum. During hydrothermal treatment, Ir nanocrystals are obtained with simultaneous reduction of GO into rGO, without addition of strong base.

After synthesis, the Ir–rGO and rGO powders were dried at 80 °C under vacuum for 24 h. To prepare the oxygen electrode, the Ir–rGO and rGO were intimately mixed in an N-methyl-2-pyrrolidone (NMP) liquid and a polyvinylidene fluoride binder (PVDF) with a weight ratio of active ingredients to PVDF of 8:2. The slurry was coated onto a gas-diffusion layer (TGP-H-030 carbon paper, Torray) and dried for 12 h at 100 °C under vacuum to remove the residual solvent.

Electrochemical testing. Electrochemical testing was carried out using a Swagelok-type cell composed of a lithium metal anode, electrolyte (1 M $LiCF_3SO_3$ in tetraethylene glycol dimethyl ether (TEGDME) impregnated into a glass fibre separator), and a porous cathode (7/16 inch diameter). The cells were sealed except for the Al grid window that exposed the porous cathode to 1 bar O_2 pressure. The electrochemical measurements were carried out using a MACCOR cycler. The discharge–charge performance was conducted in the voltage range of 2.2–4.5 V at a constant current density of 100 mA g^{-1}, and the cell was maintained in 1 bar O_2 atmosphere to avoid any negative effects of humidity and CO_2.

Characterization techniques. The phase structures of the discharge products were identified using high-energy X-ray diffraction (HE-XRD) with a wavelength of 0.11165 Å, performed at beamline 11ID-C of Sector 11 at the Advanced Photon Source (APS) of Argonne National Laboratory. The X-ray specimens were sealed with Kapton tape as a protective film in the glove box to avoid any side reactions from the air. The HE-XRD patterns were collected in the transmission mode. During the course of the measurements, a high-energy X-ray beam hit the sample horizontally, and a 2D detector (Perkin Elmer large area detector) was used to collect the X-ray diffraction profiles using transmission mode. The 2D patterns were then integrated into conventional 1D patterns (intensity versus 2θ) for final data analysis using Fit2d software.

Scanning transmission electron microscopy (TEM; JEOL JEM-2100F FEG FasTEM with an accelerating voltage of 80 kV) was employed to evaluate the morphology and particle size of the Ir catalysts and the discharge products on the porous cathodes. Spherical and chromatic aberration correction enables the microscope to reach the information limit, which is a resolution of 0.1 nm (measured by Young's fringes) at 80 kV. To prepare the TEM specimens, a dilute suspension was prepared by ultrasonically dispersing the samples in dimethyl ether for 5 min, and a drop of the suspension was placed onto a copper grid and dried. Particle size histograms were generated from the TEM images using software ImageJ. Field-emission scanning electron microscopy (SEM, Hitachi S-4700) coupled with backscattering electron imaging (BSE) was employed to determine the morphology and estimate the particle size of Ir catalyst and discharge products.

Raman spectra of the discharged cathode were obtained using a Renishaw 2000 or inVia microscope spectrometer with a HeNe laser at an exciting wavelength of 633 nm. The sample was loaded inside a glove box into a gas-tight Raman cell with a glass or quartz window. Raman spectrum collection was set up in a 180° reflective mode. Roughly 10% of the maximum 13 mW laser intensity was applied. Collection time constant setting varied from 30 s to ~100 s.

Nuclear Magnetic Resonance (NMR) spectra were collected on a Bruker Avance III 500 MHz (11.7 T) spectrometer in deuterated tetrahydrofuran (THF-d8) or deuterium oxide (D_2O). Battery samples were cycled the appropriate number of times before disassembly and rinsing with a deuterated solvent. For the samples in THF-d8, NMR samples were prepared entirely under an inert atmosphere. For samples in D_2O, the battery was disassembled under an inert atmosphere, removed from the glove box, immediately rinsed with D_2O, and sealed in an NMR tube. All 1H-NMR collections were sampled for 128 scans, manually phased, and baseline corrected before peak integration. Data collection was performed using the Bruker Topspin software (v. 3.1). Data analysis used either TopSpin (v. 3.1) or SpinWorks (V4.1.0.0).

DEMS measurements were carried out to examine the type of discharge product by measuring the evolved oxygen (O_2) molecules during the charging process, as well as calculating the e^-/O_2 ratio. The experiments were performed using an HPR40 (Hiden Analytical) instrument directly connected to a customized Swagelok battery set-up.

Theoretical methods. To study the stability of the LiO_2 system (that is, crystal, crystalline surfaces, amorphous-like thin film), its interface with a solvent and its surface growth on a intermetallic substrate (that is, Ir_3Li), we carried out Density Functional Theory (DFT) calculations with plane wave basis sets as implemented in the VASP code[35,36]. All the calculations were spin-polarized and carried out using the gradient corrected exchange-correlation functional of Perdew, Burke and Ernzerhof (PBE)[37] under the projector augmented wave (PAW) method, with plane wave basis sets up to a kinetic energy cutoff of 400 eV. The PAW method[38] was used to represent the interaction between the core and valence electrons, and the Kohn-Sham valence states (that is, 1*s* for H, 2*s* for Li, 2*s* 2*p* for C and O, 6*s* 5*d* for Ir) are expanded in plane wave basis sets. For the geometry optimization and Nudge Elastic Band calculations, the convergence criterion of the total energy was set to be within 1×10^{-5} eV for the *k*-point integration, and all the atoms and geometries were optimized until the residual forces became less than 1×10^{-2} eV Å^{-1}. For the LiO_2 crystal, the calculation was based on a mesh of $9 \times 9 \times 9$ in *k*-point grid. For both the crystalline and amorphous-like LiO_2 thin film surfaces, a *k*-point grid of $6 \times 6 \times 1$ was used. For the *Ab initio* Molecular Dynamics (AIMD) simulations, all the calculations were carried out with plane wave basis sets up to a kinetic energy cutoff of 300 eV. For the simulations of LiO_2 surface with some solvent molecules on it, the Van der Waals method of Grimme (that is, DFT-D2)[39] was used throughout both the DFT and AIMD calculations. For the simulation of the solvent, a smaller ether solvent molecule, that is, dimethoxyethane (DME) was used instead of tetraethylene glycol dimethyl ether (TEGDME) in order to reduce the computational cost. To investigate the thermodynamic stability of the system at room temperature, all the structures from the DFT optimizations were then thermally equilibrated at $T = 300$ K using AIMD simulations based on an Nose-Hoover NVT-ensemble with a time step of 1 fs.

For the *ab initio* prediction of Electron Paramagnetic Resonance (EPR) *g*-tensors of the crystalline solids LiO_2 and NaO_2, we have used the DFT plane wave code Quantum Espresso simulation package[40] in which the Gauge-Including Projector Augmented Plane Wave (GIPAW) approach[41] has been implemented. To be consistent with our VASP calculations, we employed the PBE functional and Martins-Troullier norm-conserving pseudopotentials generated by D Ceresoli (https://sites.google.com/site/dceresoli/pseudopotentials). Throughout the simulation, a plane wave energy cutoff of 150 Ry and *k*-point mesh ($9 \times 9 \times 9$) was used. Only the NaO_2 solid in *Pnnm* orthorhombic phase[42] that is thermodynamically stable at low temperature was considered in our DFT EPR calculations. For the *ab initio* prediction of the EPR *g*-tensor of the LiO_2 and NaO_2 molecules, all the calculations were obtained using the Gaussian09 code. The accuracy of the theoretical predictions are systematically tested using PBE and B3LYP functionals with the 6-31+G(2df,p) and aug-cc-PVQZ basis sets for direct comparison to the reported experimental LiO_2 and NaO_2 EPR g-tensors[43,44].

Sample size. No statistical methods were used to predetermine sample size.

34. Ha, H.-W., Kim, I. Y., Hwang, S.-J. & Ruoff, R. S. One-pot synthesis of platinum nanoparticles embedded on reduced graphene oxide for oxygen reduction in methanol fuel cells. *Electrochem. Solid-State Lett.* **14,** B70–B73 (2011).
35. Kresse, G. & Furthmüller, J. Efficiency of ab-initio total energy calculations for metals and semiconductors using a plane-wave basis set. *Comput. Mater. Sci.* **6,** 15–50 (1996).
36. Kresse, G. & Joubert, D. From ultrasoft pseudopotentials to the projector augmented-wave method. *Phys. Rev. B* **59,** 1758–1775 (1999).
37. Perdew, J. P., Burke, K. & Ernzerhof, M. Generalized Gradient Approximation made simple. *Phys. Rev. Lett.* **77,** 3865–3868 (1996).
38. Blöchl, P. E. Projector augmented-wave method. *Phys. Rev. B* **50,** 17953–17979 (1994).
39. Grimme, S. Semiempirical GGA-type density functional constructed with a long-range dispersion correction. *J. Comput. Chem.* **27,** 1787–1799 (2006).
40. Giannozzi, P. *et al.* QUANTUM ESPRESSO: a modular and open-source software project for quantum simulations of materials. *J. Phys. Condens. Matter* **21,** 395502 (2009).
41. Pickard, C. J. & Mauri, F. First-principles theory of the EPR g tensor in solids: defects in quartz. *Phys. Rev. Lett.* **88,** 086403 (2002).
42. Ziegler, M., Rosenfeld, M., Kaenzig, W. & Fischer, P. Strukturuntersuchungen an Alkalihyperoxiden. *Helvetica Physica Acta* **49,** 57–90 (1976).
43. Adrian, F. J., Cochran, E. L. & Bowers, V. A. ESR spectra and structures of $NaSO_2$ and NaO_2. *J. Chem. Phys.* **59,** 56–60 (1973).
44. Lindsay, D. M. & Garland, D. A. ESR spectra of matrix-isolated lithium superoxide. *J. Phys. Chem.* **91,** 6158–6161 (1987).